

# Tissue-like phantoms for near-infrared fluorescence imaging system assessment and the training of surgeons

## Alec M. De Grand

Beth Israel Deaconess Medical Center  
Division of Hematology/Oncology  
Boston, Massachusetts 02215

## Stephen J. Lomnes

## Deborah S. Lee

## Matthew Pietrzykowski

GE Global Research  
Niskayuna, New York 12309

## Shunsuke Ohnishi

Beth Israel Deaconess Medical Center  
Division of Hematology/Oncology  
Boston, Massachusetts 02215

## Timothy G. Morgan

GE Healthcare Biosciences  
Boston, Massachusetts 02215

## Andrew Gogbashian

## Rita G. Laurence

Brigham and Women's Hospital  
Department of Surgery  
Boston, Massachusetts 02115

## John V. Frangioni

Beth Israel Deaconess Medical Center  
Division of Hematology/Oncology and Department  
of Radiology  
Boston, Massachusetts 02215  
E-mail: jfrangio@bidmc.harvard.edu

## 1 Introduction

Living tissue has relatively low photon absorption in the near-IR (NIR) range of the electromagnetic spectrum (700 to 1000 nm). Endogenous fluorophores are strong contributors to autofluorescence in the UV and visible regions of the spectrum, but are significantly weaker in the NIR. Hence, from an absorbance and autofluorescence standpoint, NIR light has distinct advantages. Scatter is significant at all wavelengths, and is a complex function of tissue composition (discussed in Ref. 1). However, for many tissues, the absolute value of scatter tends to be lower in the NIR.

Recently, there has been a dramatic rise in the publication of imaging systems that exploit NIR light, and in some cases, exogenous NIR fluorophores. The three basic types of imaging systems are steady state (also known as continuous wave

**Abstract.** We demonstrate how to construct calibrated, stable, and inexpensive tissue-like phantoms for near-IR (NIR) fluorescence imaging applications. The bulk phantom material is composed of gelatin, intralipid, hemoglobin, and indocyanine green (ICG). Absorbance, scatter, background fluorescence, and texture can be tuned as desired. NIR fluorescent inclusions are comprised of ICG-labeled polystyrene divinylbenzene beads and Pam78-labeled hydroxyapatite crystals. The former mimic tumor masses of controllable size and contrast agent concentration, and the latter mimic microcalcifications in breast cancer. NIR-fluorescent inclusions can be positioned precisely in phantoms, with one or more regions having different optical properties, and their position can be verified independently using microcomputed tomography. We demonstrate how these phantoms can be used to calibrate and compare imaging systems, and to train surgeons to operate under NIR fluorescence image guidance. © 2006 Society of Photo-Optical Instrumentation Engineers. [DOI: 10.1117/1.2170579]

Keywords: near-infrared fluorescence; optical imaging; phantoms; indocyanine green; hydroxyapatite; surgical training.

Paper 05042R received Feb. 14, 2005; revised manuscript received Aug. 31, 2005; accepted for publication Oct. 6, 2005; published online Feb. 10, 2006.

or cw), time domain, and frequency domain. Within each, source/detector geometry can be based on point or area illumination, and point or area detection, leading to over 12 different imaging system configurations (reviewed in Ref. 2).

Paralleling the explosion of imaging systems is a similar one for exogenous NIR fluorophores. Several comprehensive reviews of NIR fluorophores used for *in vivo* imaging were recently published.<sup>3-5</sup> Briefly, NIR fluorescent contrast agents are now available for quantitation of vascular mapping, tissue perfusion, tissue calcification, protease activity, cell injury, tissue response to injury, and for specific applications such as sentinel lymph node mapping and tumor imaging.

As imaging systems and contrast agents converge, there is an increasing need for standardized NIR fluorescent phantoms that can be compared among laboratories, and that assist with the training of surgeons and technologists. Cubeddu et al.<sup>6</sup> described agar-based phantoms utilizing intralipid for scattering and India ink for absorption. Wagnieres et al.<sup>7</sup> described

Address all correspondence to John V. Frangioni, Beth Israel Deaconess Medical Center, Division of Hematology/Oncology and Department of Radiology, Boston, Massachusetts 02215. Tel.: 617-667-0692; Fax: 617-667-0981; E-mail: jfrangio@bidmc.harvard.edu

agarose-based phantoms containing silica powder and intralipid for scattering and India ink and erythrocyte concentrate for absorption. The former optical phantom utilizes non-physiological absorbers, the latter is difficult to construct, and both utilize a galactose polymer as base material. Quan et al.<sup>8</sup> and Kelly et al.<sup>9</sup> utilized gelatin derived from the hydrolysis of vertebrate connective tissue as a phantom base material for photoacoustic and radiation dosimetry studies, respectively. Two recent studies<sup>10,11</sup> utilized gelatin-based phantoms for NIR fluorescence studies; however, neither describes the construction of precise NIR fluorescent inclusions or a general-purpose phantom platform. Other approaches to NIR imaging phantoms include hard resin or soft room temperature vulcanizing (RTV) silicon materials<sup>12</sup> into which holes are drilled; however, this system is inflexible with respect to inclusion size, placement, and geometry, and multiple interfaces are formed at each hole site. In this paper, we demonstrate how to construct simple, yet stable, gelatin-based phantoms that can be tailored to the optical properties of various tissues using readily available materials. We also describe two different types of NIR fluorescent inclusions that simulate tumor spheroids and/or breast cancer microcalcifications.

## 2 Materials and Methods

### 2.1 Reagents

National Formulary (NF) grade gelatin (catalog #EM-GX0048-1) was from VWR (West Chester, Pennsylvania). Sterile Intralipid™ (20% w/v) was purchased from Baxter (Deerfield, Illinois). Bovine hemoglobin (catalog #H-2625) and indocyanine green (ICG; catalog #I-2633) were from Sigma (St. Louis, Missouri). AG1-X8 anion exchange resin (catalog #140-1422) was from Bio-Rad (Hercules, California). Pam78 was prepared as described (see Zaheer et al.<sup>13</sup>). The 100- $\mu\text{m}$  hydroxyapatite (HA) crystals (catalog #391947) were from Calbiochem (La Jolla, California).

### 2.2 Phantom Mixture Construction

The buffer for all phantoms was Tris-buffered saline (TBS) composed of 50 mM Tris, pH 7.4, and 150 mM sodium chloride. Sodium azide was added to a final concentration of 0.1% (15 mM; TBS/azide) to bind methemoglobin, block reoxygenation, and to act as a preservative. Gelatin was suspended at the desired concentration (% w/v) in TBS (GTS), and warmed to 37 to 50°C with constant stirring until completely dissolved. GTS was then cooled to 25°C and the desired amounts of hemoglobin and Intralipid added, with constant stirring. Solidification of the GTS mixture should be performed as rapidly as possible to avoid separation of the Intralipid. We found that pouring the room temperature solution into the desired prechilled mold at 4°C will minimize this effect. Depending on the size and shape of the mold, solidification should take 5 to 20 min.

### 2.3 NIR Fluorescent Inclusions

NIR fluorescent inclusions were made using ICG-labeled polystyrene divinylbenzene beads (AG1-X8) or Pam78-labeled hydroxyapatite crystals. These latter inclusions were used to simulate microcalcifications found in breast cancer.<sup>14</sup> The concentration of fluorophore associated with each inclu-

sion was measured precisely, and expressed as “ICG equivalence” (defined in the following). Beads were sieved twice to a diameter of  $1000 \pm 100 \mu\text{m}$  using a 20-mesh (850- $\mu\text{m}$  square holes) brass sieve (VWR catalog #57334-112). For bead loading, 10 mM ICG in DMSO was diluted in TBS to twice the desired loading concentration and mixed 1:1 with a 50% bead slurry, vortexed for 3 s, incubated 20 min, and washed  $4 \times$  with TBS. Pam78 was loaded onto HA in a similar fashion. For dual-labeling with iodine contrast and ICG, 60% iohalamate meglumine (stock concentration 2.22 M iodine; Conray™, Mallinckrodt, St. Louis, Missouri) was diluted in TBS to a final iodine concentration of 88.8 mM prior to the addition of ICG and bead loading. Prior to embedding into phantoms, NIR fluorescent inclusions were calibrated against ICG standards in DMSO having the same path length to determine their “ICG equivalence” (see later).

Fluorescent inclusions, having ICG equivalence<sub>(725–775 nm, 5 mW/cm<sup>2</sup>, >795 nm, 1 mm)</sub> from 0 to 5  $\mu\text{M}$ , could be varied in size from 75 to 1000  $\mu\text{m}$ . The 3-D positioning of fluorescent inclusions was verified independently using an eXplore Locus microcomputed tomography system (GE Healthcare Biosciences, Waukesha, Wisconsin) to within  $\pm 90 \mu\text{m}$ .

### 2.4 Phantom Construction

For phantoms with uniform bulk optical properties, a mold is filled and gelled to the desired level of the inclusion, then the inclusions are mixed with a 30°C phantom solution (5 to 100  $\mu\text{L}$  depending on inclusion) and pipetted onto the surface of the solidified mold. The warmth of the solution softens the top of the mold and allows the inclusion solution to adhere to the surface. Once the inclusion solution has set, more of the same warm phantom mix can be poured on top, thus removing any interfaces. Different levels of the same phantom can have different inclusions inserted into it without having to create separate molds for each level (Fig. 1). Moreover, various regions of the same phantom can have different properties, without artificial refractive interfaces.

Phantoms with different optical properties in different compartments can be produced by placing smaller molds inside the larger main mold. These smaller submolds can then be filled with different phantom mixtures, with the inclusions inserted into these molds in a similar manner as already described. Alternatively, different compartments can be constructed separately, then added to the main mold using warm gelatin as already described for inclusions. The remaining gaps are filled in using the desired warm phantom mixture. To minimize glare in color images due to uneven surfaces, complex phantoms are often covered with an additional 1- to 3-mm layer of GTS, which has negligible effect on scatter and absorption. Once a phantom has been constructed, it can be stored for long periods in a sealed container, preferably a humidified one, at 4°C.

### 2.5 Optical Measurements

Absorbance spectrometry was performed using a 1-cm path length quartz cuvette (Starna, Atascadero, California), HR2000 fiber optic spectrometer and a DH2000-BAL light source (Ocean Optics, Dunedin, Florida). Spectral reflectance measurements were made using the same spectrometer and

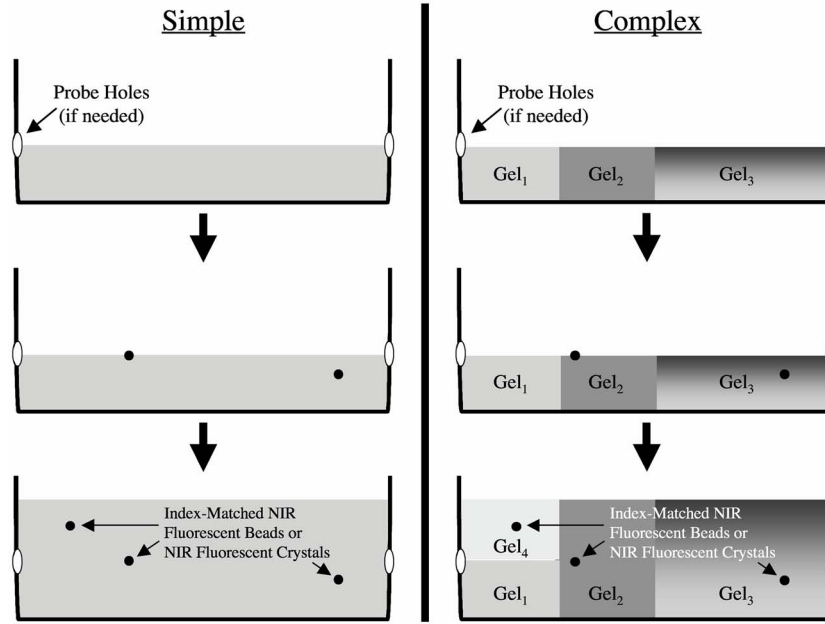


**Fig. 1** Tissue-like phantoms for NIR fluorescence imaging. By choosing the scatter, absorbance, and background fluorescence of the phantom medium, simple (left) or complex (right) phantoms can be created. In complex phantoms, optical properties can be varied in three dimensions, including the use of gradients (e.g., Gel<sub>3</sub>), without refractive interfaces. For optical tomography, probe holes are predrilled and sealed before filling, or the container is coated with vegetable oil for easy removal of the entire phantom. Fluorescent inclusions can be placed at any position in 3-D within the phantom.

light source equipped with a R400-7-VIS/NIR probe (Ocean Optics), and normalization was performed using a homogeneously reflecting surface.

Absolute absorption and reduced scattering were measured on a Lambda 19 (Perkin Elmer, Boston, Massachusetts) UV/Vis/NIR spectrophotometer equipped with a 150-mm integrating sphere. For long-term stability experiments, phantoms were measured in this apparatus over a 4-week period, being stored at 4°C in a humidified chamber on intervening days. To assess diffusion during long-term stability testing, samples were prepared between two 2- × 3-in. glass slides, and were composed of a central 0.5- × 1.385-in. rectangle (area of measurement) of one material with the remaining periphery composed of a second material. The edges were sealed with epoxy. The scattering and absorbing properties of samples were computed using the inverse adding-doubling method<sup>15</sup> from 400 to 1000 nm (the algorithm is available for download at <http://omlc.ogi.edu/software/iad/>).

We compared the results provided by the integrating sphere and inverse adding-doubling method to Mie theory using samples of known properties. We purchased 903-nm polystyrene (PS) beads (Catalog #3900A) from Duke Scientific (Palo Alto, California). The Mie theory calculator was accessed at [http://omlc.ogi.edu/calc/mie\\_calc.html](http://omlc.ogi.edu/calc/mie_calc.html). Inputs to the calculator included an index of refraction of 1.33; real indices of refraction of spheres of 1.6, 1.582, 1.575, and 1.57 for 400, 600, 800, and 1000 nm, respectively; imaginary indices of refraction of  $-0.00045$ ,  $-0.0008$ ,  $-0.001$ , and  $-0.002$  for 400, 600, 800, and 1000 nm, respectively; 200 angles; and, a density of 0.0073 spheres/ $\mu\text{m}^3$  (Ref. 16).

Fluorescence spectrometry was performed with a 225- $\mu\text{L}$ , three-sided quartz cuvette (Starna), HR2000 fiber optic spec-

trometer and CUV-ALL-UV four-way cuvette holder (Ocean Optics), and 770-nm NIR laser diode light source (Electro Optical Components, Santa Rosa, California) set to 8 mW with output through a 300- $\mu\text{m}$  core diameter, numerical aperture (NA) 0.22 fiber (Fiberguide Industries, Stirling, New Jersey).

Intraoperative NIR fluorescence imaging was performed as described in detail previously,<sup>17</sup> using filtered (Chroma #HHQ750/50x) 725- to 775-nm NIR excitation light, and custom light collection optics equipped with a long-pass ( $\geq 795$  nm) emission filter (Chroma #HQ795LP).

## 2.6 Quantification of Autofluorescence in Living Tissues

Animal protocols were in accordance with Institutional Animal Care and Use Committee Guidelines. Thirty-five-kilogram adult male Yorkshire pigs ( $n=3$ ) were purchased from E.M. Parsons and Sons (Hadley, Massachusetts). All animals acclimated to the animal facility for at least 48 h prior to experimentation. Pig anesthesia was induced with 4.4 mg/kg intramuscular Telazol (Fort Dodge Labs, Fort Dodge, Iowa) and anesthesia maintained through a 7-mm endotracheal tube with 1.5% isoflurane/98.5% O<sub>2</sub> at 5 L/min.

Tissues and organs were surgically exposed, then imaged using NIR excitation light of 725 to 775 nm, with an excitation fluence rate of 5 mW/cm<sup>2</sup> (as measured with a calibrated Orion-TH digital light power meter equipped with an Orion model 2A-SH thermopile detector head). In each field of view, and on nonabsorbing and nonreflecting black matte paper (Canson Mi-Teintes, Stygian Black #425), were placed 1-mm path length ICG standards in DMSO of 0, 31, 63, 125,

250, 500, 1000, and 2000 nM, and calibration curves were created for camera exposure times of 10, 34, 67, 134, 500 and 1000 ms. From these six curves, the average autofluorescence of the tissue or organ under study was calculated, and expressed as ICG equivalence<sub>(725–775 nm, 5 mW/cm<sup>2</sup>, >795 nm, 1 mm)</sub>.

After each study, anesthetized animals are euthanized by rapid intravenous injection of 10 mL of Fatal-Plus (Vortech Pharmaceuticals, Dearborn, Michigan). This method of euthanasia is consistent with the recommendations of the Panel on Euthanasia of the American Veterinary Medical Association.

### 3 Results

#### 3.1 Preparation of Phantoms

Phantoms were prepared in covered plastic food storage containers of the desired size and geometry. The basic building block is a gelatin-containing medium having the desired absorbance, scatter, and background fluorescence. Absorbance of the medium is controlled by the concentration of oxy- and deoxyhemoglobin (the ratio of which can be adjusted using azide), and/or other biomolecules. Scatter is controlled by the concentration of Intralipid, with virtually no contribution from the gelatin, even at high concentrations.

#### 3.2 Characterization of Phantom Optical Properties

Optical properties of the phantoms were measured using an integrating sphere as described in Sec. 2. Validation of the inverse adding-doubling algorithm employed was performed by comparing results of Mie scattering theory with calibrated polystyrene beads of defined optical properties. As shown in Fig. 2(A), theoretical and empirical values for  $\mu_A$ ,  $\mu'_S$ , and anisotropy were closely correlated over the wavelength range 400 to 1000 nm. Optical properties of the various phantom components over this wavelength range are shown in Fig. 2(B) (various concentrations of intralipid in 10% GTS) and Fig. 2(C) (complete phantom). Note that our values for  $\mu'_S$  of 1% Intralipid in GTS are approximately twofold lower than previously published values for 1% Intralipid in water, which likely reflects lot-to-lot variation in particle size. We also found unexpectedly high scatter at 400 nm in the presence of concentrated Hb [Fig. 2(C)], possibly due to Rayleigh scatter from the Hb molecules themselves. Absorbance of the phantom is controlled by the hemoglobin concentration, with a negligible contribution by gelatin at blue wavelengths [Fig. 2(D)].

Varying the concentration of ICG in the medium controls background fluorescence, and also adds a NIR component to absorption [Fig. 2(E)]. Background fluorescence could be varied from 0 to 1.4  $\mu\text{M}$  ICG equivalence<sub>(725–775 nm, 5 mW/cm<sup>2</sup>, >795 nm, 1 mm)</sub> by varying ICG concentration from 0 to 1  $\mu\text{M}$ . The enhancement of ICG quantum yield after adsorption to proteins, such as gelatin, is well known.<sup>18</sup>

The absorbance, scatter, and background fluorescence of the phantom can be varied in three dimensions; hence, complex phantoms having any desired optical properties and geometry can be constructed inexpensively and easily using this system (Fig. 1; see also Fig. 6 in Sec. 3.8). Using the same base material for all compartments minimizes refractive inter-

faces. Interestingly, phantoms can be remelted, NIR fluorescent inclusions retrieved, and all materials recycled into new phantoms as needed.

#### 3.3 Characterization of Phantom Homogeneity

Phantom homogeneity was tested by taking 20 full-spectrum (400 to 1000-nm) reflectance measurements each in the *X* and *Y* directions, at 5-mm intervals. As shown in Fig. 2(F), variation over this 10-cm distance, in either direction, was less than 2%.

#### 3.4 Characterization of Phantom Stability

The stability of the phantom over time was measured at 400, 600, 800, and 1000 nm over a 4-week period. Shown in Fig. 3(A) is the variation in transmission, and in Fig. 3(B), the variation in reflectance. At wavelengths from 600 to 1000 nm, there was virtually no change in optical properties of the phantom components. However, at 400 nm and starting at approximately 2 weeks, there was evidence of Hb transition from the oxy-, deoxy-, and possibly met-Hb states, as well as evidence of diffusion of Hb within the phantom. Although these results should have no impact on NIR fluorescence experiments, use of multicompartment phantoms for measuring Hb concentration over periods greater than 2 weeks must be performed with these results in mind.

#### 3.5 Concept of “ICG Equivalence”

To solve the problem of extrapolating results from one embedded fluorescent inclusion to another, and from one phantom to another, we report all fluorescence emissions in terms of “ICG equivalence,” that is, the measured fluorescence emission over a defined wavelength range, excited with NIR light of a defined wavelength and fluence rate, which is equivalent to an ICG standard in DMSO of a defined path length and concentration. For simplicity, the following notation is employed: ICG equivalence<sub>Excitation Wavelength(s), Fluence Rate, Emission Wavelength(s), Path Length</sub>; DMSO is one of the few solvents in which ICG is stable,<sup>19</sup> and for which an absolute quantum yield (13%) has been reported.<sup>20</sup> Hence, by expressing measured fluorescence as ICG equivalence, the performance of virtually any other NIR fluorophore, with similar excitation/emission wavelengths, can be extrapolated. For example, IRDye78 (LI-COR, Lincoln, Nebraska), an NIR fluorophore commonly used by our laboratory, has a quantum yield of  $\approx 14\%$  in aqueous buffer,<sup>21</sup> hence fluorescent inclusion results expressed as ICG Equivalence would be roughly equivalent to the expected performance of IRDye78.

#### 3.6 Autofluorescence of Living Tissue

Living tissue has a low, but measurable, autofluorescence, which must be known before construction of a phantom with the proper amount of “background” fluorescence. Figure 4 shows the autofluorescence of virtually every tissue and organ in the body, expressed as ICG equivalence<sub>(725–775 nm, 5 mW/cm<sup>2</sup>, >795 nm, 1 mm)</sub>. The path length of the ICG standards in DMSO used to make these measurements must be specified since the reflectance imaging system employed in these studies is sampling an unknown depth of tissue. Since fluorescence emission often scales nonlinearly

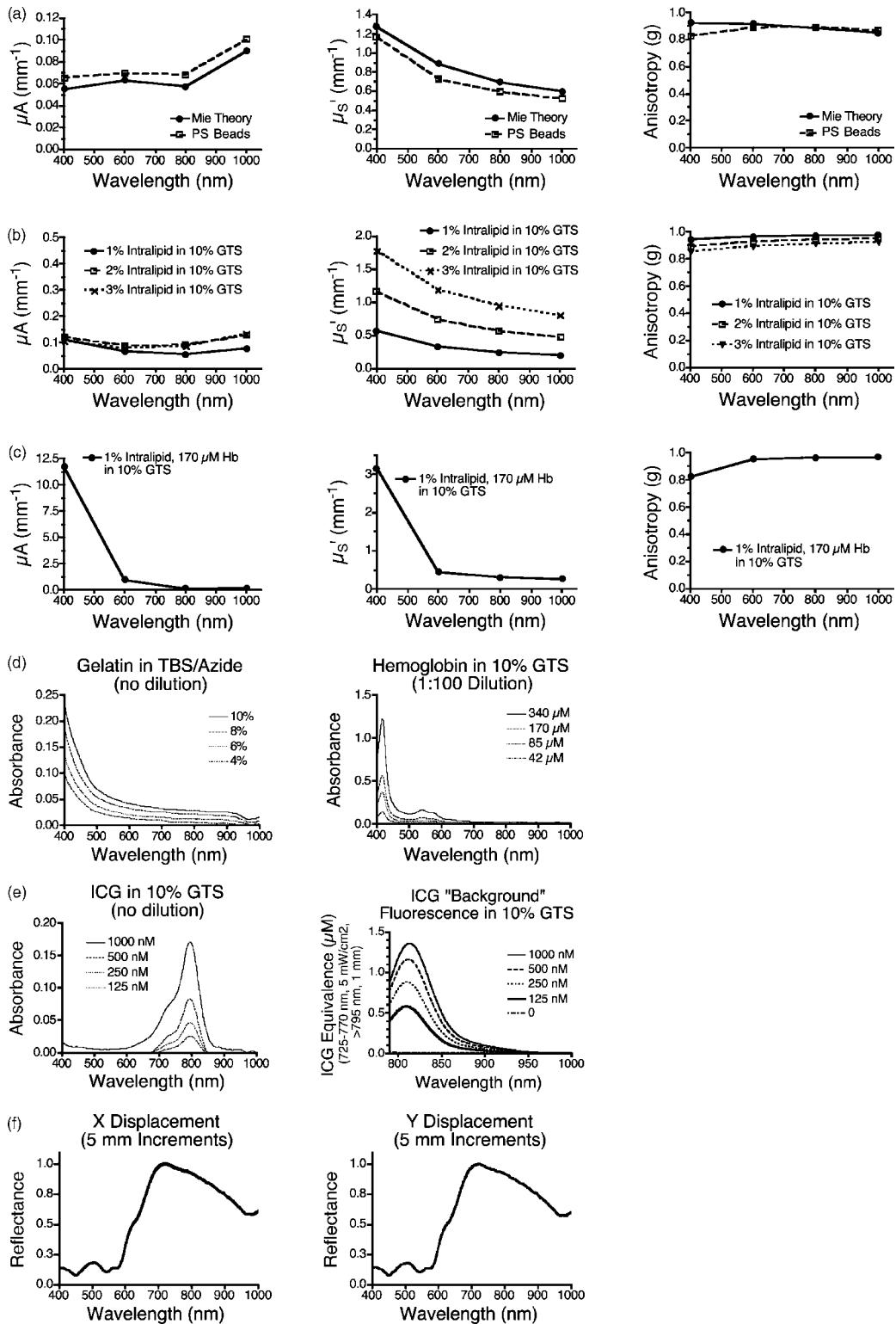


**Fig. 2** Optical characterization of phantom components. (A) Validation of the employed inverse adding-doubling method by comparing measurements using polystyrene (PS) beads of defined optical properties (PS beads) to Mie scattering theory (Mie theory). Shown are  $\mu_A$  (left),  $\mu_s'$  (middle), and anisotropy (right). (B) Optical properties of various Intralipid concentrations as measured using an integrating sphere and the inverse adding-doubling method. Shown are  $\mu_A$  (left),  $\mu_s'$  (middle), and anisotropy (right). (C) Optical properties of a typical phantom mixture composed of 1% Intralipid and 170  $\mu$ M Hb in 10% GTS. This composition most closely matches scattering human tissue with an 8% blood volume. Shown are  $\mu_A$  (left),  $\mu_s'$  (middle), and anisotropy (right). (D) Absorbance of various gelatin concentrations in TBS/azide (left), and Hb in 10% GTS (right; diluted 1:100 in TBS/azide prior to measurement). (E) Absorbance (left) and "background" fluorescence (ICG equivalence<sub>(725-775 nm, 5 mW/cm<sup>2</sup>, >795 nm, 1 mm)</sub>, described in text; right) of ICG in 10% GTS. (F) Homogeneity of a 1% Intralipid/170  $\mu$ M Hb phantom in 10% GTS measured in 5 mm increments in the X (left) and Y (directions), over a total distance of 10 cm. Shown are the mean  $\pm$ SEM (standard error of the mean) of the 20 reflectance spectra at each wavelength from 400 to 1000 nm.

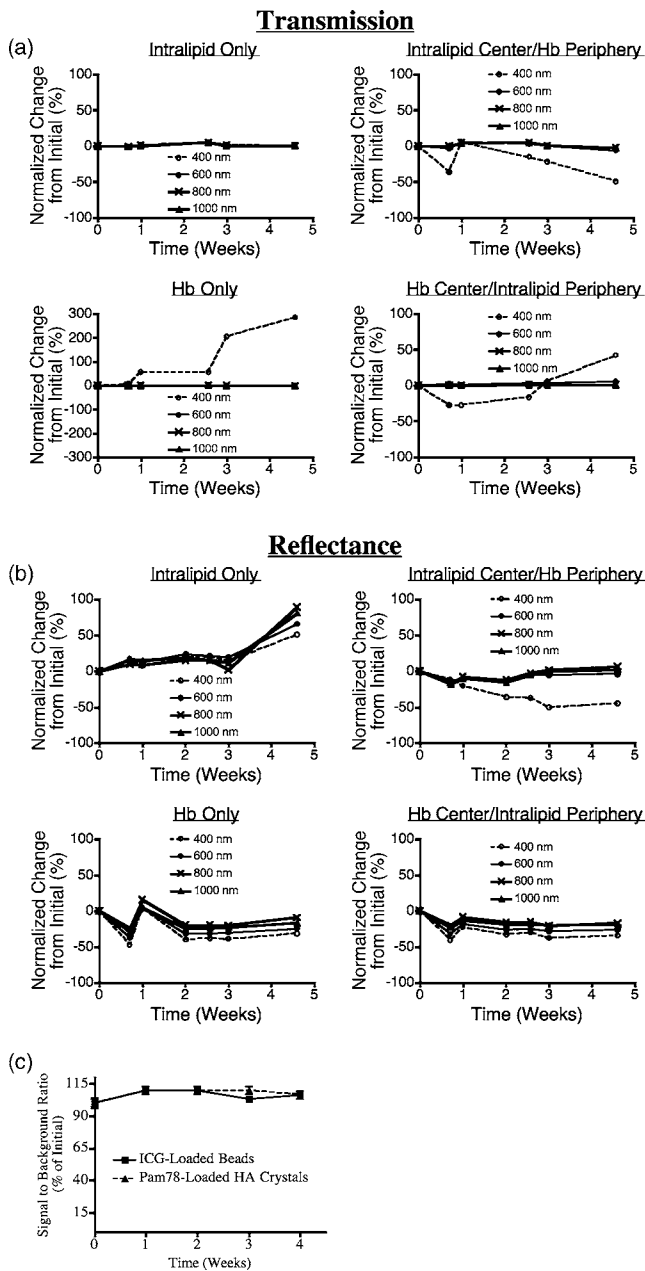


**Fig. 3** Long-term stability of tissue-like phantoms and their NIR fluorescent inclusions. (A) Transmission over a 4-week interval for 1% Intralipid in 10% GTS (top left), 1% Intralipid in a central location with Hb around the periphery, both in 10% GTS (top right), 170  $\mu\text{M}$  Hb in 10% GTS (bottom left), and 170  $\mu\text{M}$  Hb in a central location with 1% Intralipid around the periphery, both in 10% GTS (bottom right). (B) Reflectance over a 4-week interval for the samples described in (A). (C) Stability of NIR fluorescent inclusions. NIR fluorescent beads and HA inclusions, each with a 1  $\mu\text{M}$  ICG equivalence<sub>(725–775 nm, 5 mW/cm<sup>2</sup>, >795 nm, 1 mm)</sub>, were placed randomly throughout a phantom (1% Intralipid and 170  $\mu\text{M}$  Hb in 10% GTS) at a depth of 5 mm, and measurements were taken weekly. Between measurements, the phantom was sealed tightly in a storage container at 4°C. On the ordinate is signal-to-background ratio (SBR) expressed as mean  $\pm$  SEM.

with inclusion size, it is best to match the inclusion size to the typical tumor size of the model system employed. The values in Fig. 4 can be used to add the appropriate level of phantom

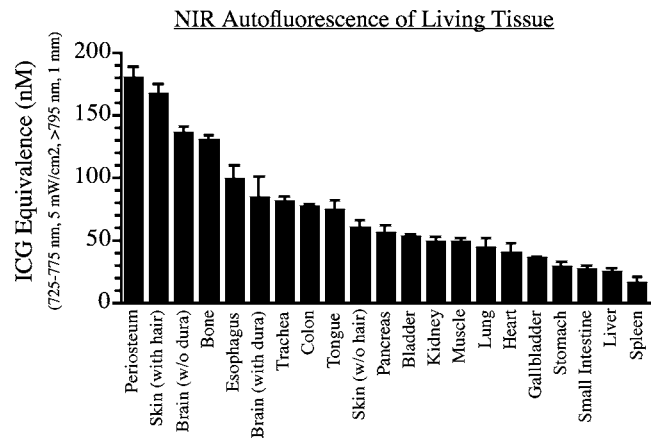


**Fig. 4** Relative and absolute NIR autofluorescence of living tissues. ICG equivalence of major tissue types of the pig. Results shown are the average of three separate animals (mean  $\pm$  SEM), and are expressed as ICG equivalence<sub>(725–775 nm, 5 mW/cm<sup>2</sup>, >795 nm, 1 mm)</sub> (nM).

background fluorescence for the tissue type under study. This is especially important since the relative autofluorescence of different tissues varies by over ninefold.

### 3.7 NIR Fluorescent Inclusions

Similar to the submillimeter radiosciintigraphic calibration sources previously reported by our group,<sup>22</sup> the beads used in this study are available in wet bead diameters from 45 to 1180  $\mu\text{m}$ , which can be sieved to any desired size, and are also available with cross-linking ranging from 2 to 8%. The latter value is important, since it determines the exclusion limit of the bead interior. The 8% bead used in this study does not exclude 775-Da ICG, resulting in relatively homogeneous fluorescence over the entire volume of the bead. Bead loading with ICG is distinctly nonlinear (Fig. 5), with stacking and quenching limiting the ICG Equivalence<sub>(725–775 nm, 5 mW/cm<sup>2</sup>, >795 nm, 1 mm)</sub> per bead to approximately 4.2  $\mu\text{M}$ . Due to high viscosity, Conray<sup>TM</sup> iodine contrast is diluted to 88.8 mM prior to bead loading. As expected, iodine contrast shifts the ICG loading curve shown in Fig. 5 to the right (data not shown), emphasizing again the importance of confirming the ICG equivalence of each fluorescent inclusion prior to placement in the phantom.

A second NIR fluorescent inclusion used in this study is HA crystals loaded with Pam78, a NIR fluorescent derivative of the bisphosphonate pamidronate.<sup>13</sup> Pam78 has been used previously for *in vivo* imaging of sites of osteoblastic activity and the simulated calcification of breast cancer.<sup>23</sup> Pam78-loaded HA is an ideal fluorescent inclusion for tissue-like phantoms since it has biologic and medical relevance, and can be loaded with physiologically relevant concentrations of fluorophore (Fig. 5).

The stability of the NIR fluorescent inclusions was tested over 4 weeks with no significant changes in fluorescence emission found [Fig. 3(C)]. Given the stability of the base material and NIR fluorescent inclusions, phantoms could theoretically be shipped to any other laboratory for calibration or comparative assessment of different imaging systems.

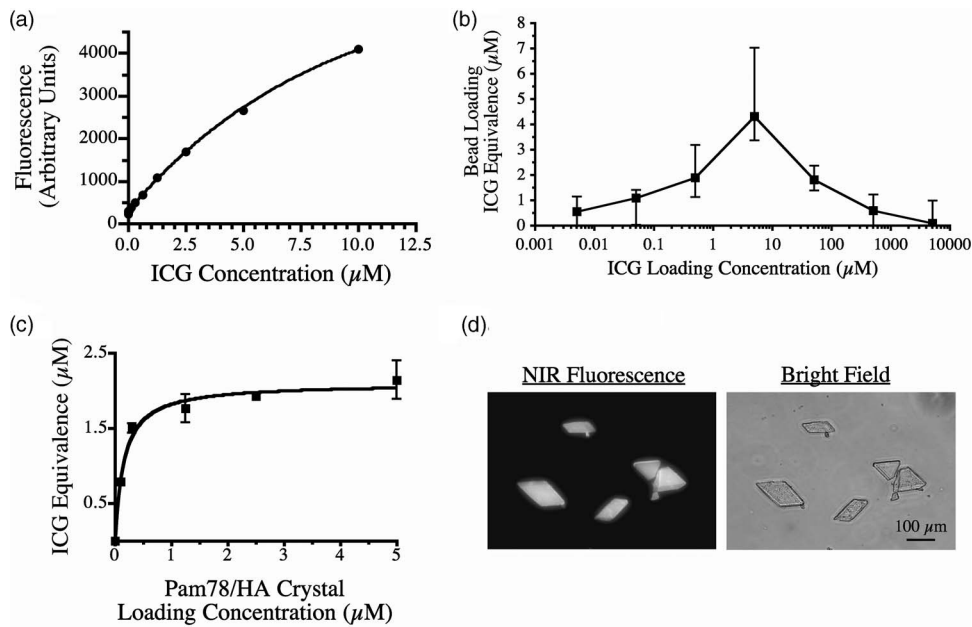


**Fig. 5** Characterization of NIR fluorescent inclusions. (A) 0.79  $\mu\text{L}$  ICG standards in DMSO. (B) ICG equivalence $_{(725-775 \text{ nm}, 5 \text{ mW/cm}^2, >795 \text{ nm}, 1 \text{ mm})}$  [ $\mu\text{M}$ ; mean  $\pm$  SD (standard deviation)] of individual 1-mm (0.79  $\mu\text{L}$ ) ICG-loaded anion exchange beads expressed as a function of loading concentration. (C) ICG equivalence $_{(725-775 \text{ nm}, 5 \text{ mW/cm}^2, >795 \text{ nm}, 1 \text{ mm})}$  ( $\mu\text{M}$ ; mean  $\pm$  SD) of individual 100  $\mu\text{m}$  HA crystals loaded with Pam78 and calibrated against 100- $\mu\text{m}$  path length ICG standards in DMSO. (D) 100- $\mu\text{m}$  Pam78-labeled HA crystals loaded with a 1  $\mu\text{M}$  ICG equivalence $_{(725-775 \text{ nm}, 5 \text{ mW/cm}^2, >795 \text{ nm}, 1 \text{ mm})}$  as viewed on a NIR fluorescence microscope.

### 3.8 Imaging System Calibration and Performance Assessment

One of the major uses for these phantoms is in assessing the performance of tomographic and reflectance imaging systems. This is illustrated in Fig. 6 using a NIR fluorescence imaging system designed for large animal and human studies.<sup>17</sup> The complex phantom shown is particularly relevant to *in vivo* conditions, where nearby tissues have distinctly different optical properties. The SBR, as well as visual discrimination of the inclusions, could be measured as a function of fluence rate, system optics, and camera integration time, and the precise 3-D position of inclusions measured using microcomputed tomography [Fig. 6(C)]. Of note, radiodense HA crystals require no additional contrast to be colocalized by microcomputed tomography (data not shown).

### 3.9 Training in Imaging System Operation and Image-Guided Surgery Using NIR Fluorescent Phantoms

We previously described an intraoperative NIR fluorescence reflectance imaging system that enables the surgeon to view surgical anatomy (via color video) and tumor or lymph node location (via NIR fluorescence) simultaneously, in real-time, and without moving parts<sup>17,21</sup> [see also Fig. 6(B)]. As with any new imaging system, there is a learning curve associated with use of system software, and the surgeon must also be trained at NIR fluorescence-guided dissection, resection, and postresection inspection of the surgical field. The phantoms described in this paper may prove useful for such training and should permit quantitative assessment of surgical expertise.

Figure 7 shows a breast-shaped phantom with optical properties similar to the human breast. Embedded within

the breast are nine 1-mm NIR fluorescent beads, corresponding to a tumor of approximately  $8 \times 10^5$  cells (discussed later in the paper). Each bead has an ICG equivalence $_{(725-775 \text{ nm}, 5 \text{ mW/cm}^2, >795 \text{ nm}, 1 \text{ mm})}$  of 1  $\mu\text{M}$ , corresponding to approximately  $6 \times 10^5$  fluorophore molecules per cell. Given the close index matching between inclusions and phantom, it is virtually impossible to find inclusions using the naked eye or color video enhancement. Using the NIR fluorescence channel, however, the inclusions are easily found (presurgery), and the surgeon can then resect the desired inclusion (resection) and inspect the field to ensure completeness (postresection).

## 4 Discussion

In this paper, we demonstrate how to construct simple, inexpensive phantoms for NIR fluorescence imaging applications. The significant advantages of these phantoms include complete control over geometry and optical properties, the ability to create both simple and complex conditions, the ability to independently confirm the 3-D position of fluorescent inclusions using computed tomography, the ability to incorporate any pigmented biomolecule (e.g., hemoglobin), high stability over time in the NIR, no artificial interface between volumes having different optical properties or between fluorescent inclusions and medium, and the representation of fluorescence emission as “ICG equivalence.” Moreover, these phantoms should be compatible with tomographic imaging systems having either circular<sup>24–26</sup> or planar<sup>27</sup> geometry (detailed in Fig. 1).

Interestingly, cross-linking of the phantoms for various periods of time (typically 1 to 2 h) with various concentrations of glutaraldehyde (0.1 to 1%) enables fine-tuning of their me-

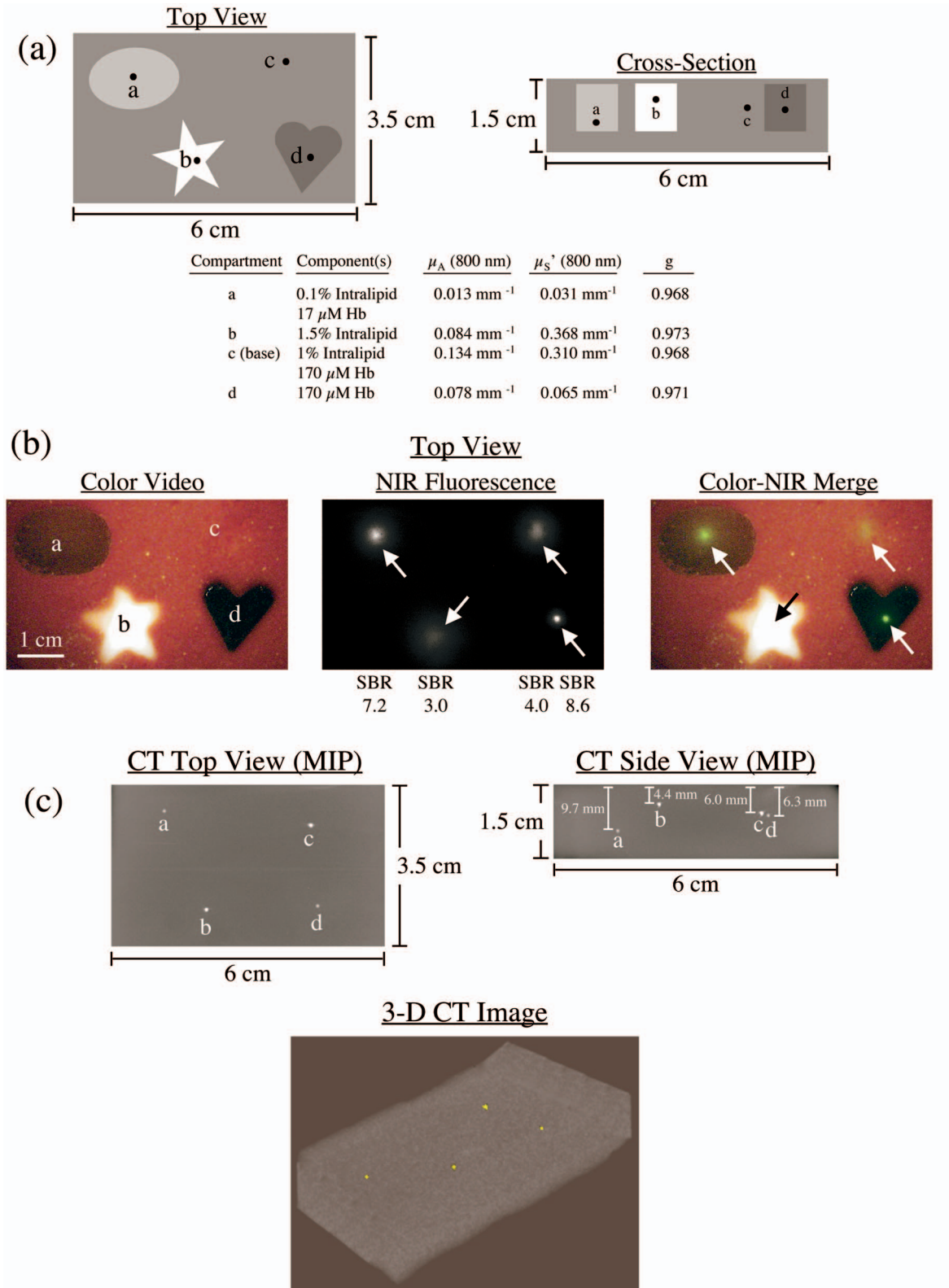


**Fig. 6** Complex phantom for the calibration and assessment of a NIR fluorescence imaging system, and independent confirmation by microcomputed tomography. (A) Schematic design of a complex phantom containing four compartments with optical properties shown in the table. Each compartment contained a 1 mm diameter bead of 880 nm ICG equivalence<sub>(725–775 nm, 5 mW/cm<sup>2</sup>, >795 nm, 1 mm)</sub> and 88.8 mM Conray™ placed at the desired depth. (B) Simultaneous color video/ NIR fluorescence imaging (top view) of the phantom using a NIR excitation fluence rate of 5 mW/cm<sup>2</sup> and 100-ms exposure time. Shown are color video (left), NIR fluorescence (middle), and a pseudocolored (lime green) merge of the two (right). All pixel values were within the linear range of the NIR camera. Below each NIR fluorescent bead (arrows) is shown its SBR. (C) Confirmation of precise position of NIR fluorescent inclusions using microcomputed tomography. Shown are the maximum intensity projections (MIPs) for top view and side view, along with a 3-D rendering of the phantom with beads in yellow.

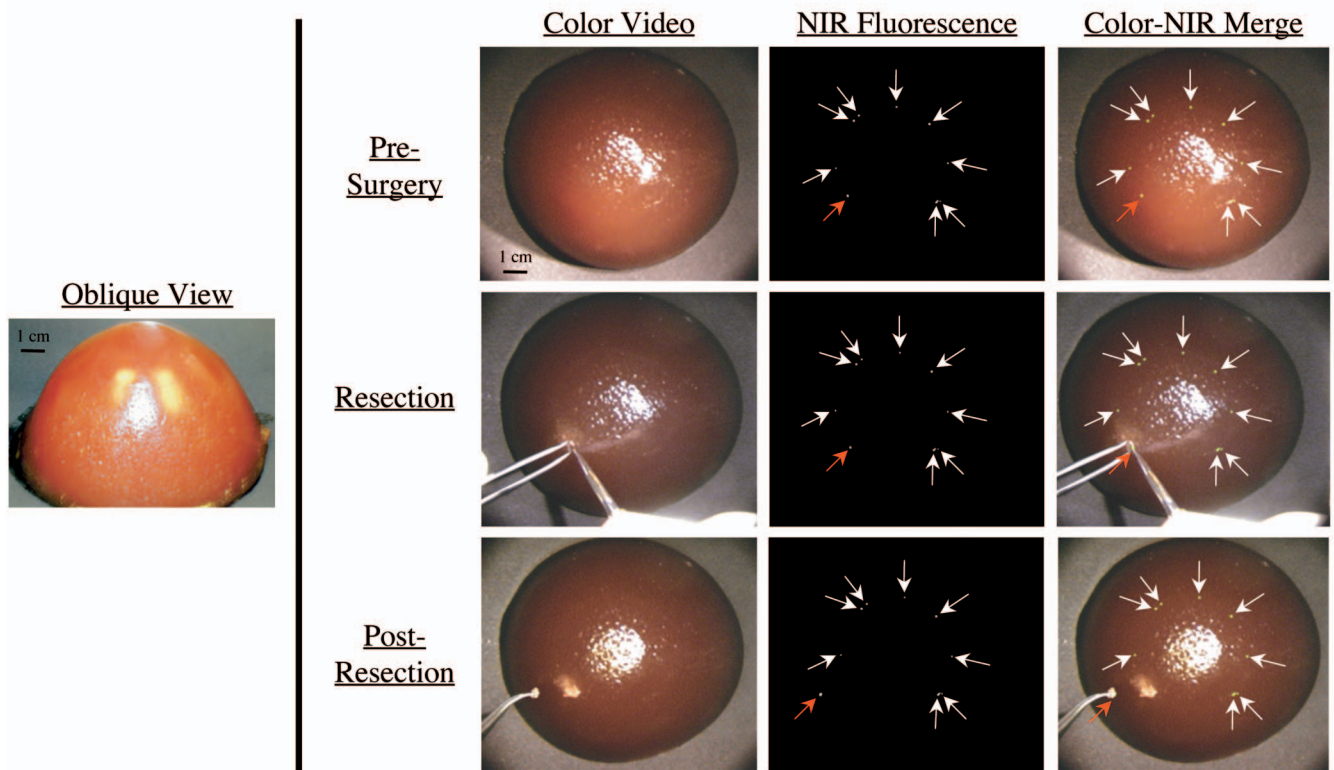


**Fig. 7** Training in image-guided surgery using NIR fluorescent phantoms. Nine 1-mm beads (each approximating a collection of  $8 \times 10^5$  cells; arrows) with a  $1 \mu\text{M}$  ICG equivalence<sub>(725–775 nm, 5 mW/cm<sup>2</sup>, >795 nm, 1 mm)</sub> were placed concentrically, and 0.5 cm below the surface, of a breast-shaped phantom (see oblique view). The phantom composition was 10% gelatin, 1% Intralipid, and  $17 \mu\text{M}$  hemoglobin, corresponding to  $\mu_A = 0.056 \text{ mm}^{-1}$ ,  $\mu'_s = 0.310 \text{ mm}^{-1}$ , and  $g = 0.968$  at 800 nm. Shown is NIR fluorescence image-guided resection of one (red arrow) of the otherwise invisible beads using a scalpel and forceps. NIR fluorescence images have identical exposure times (100 ms) and normalizations.

chanical properties, with more highly cross-linked phantoms remarkably similar to living tissue when cut with a scalpel. Glutaraldehyde presumably cross-links both the buffer (Tris) and protein components of the phantom, and of course, requires remeasurement of all optical properties. Glutaraldehyde does not appear to affect significantly NIR fluorescence emission from either bead/ICG or HA/Pam78 inclusions (data not shown).

The fluorescent inclusions described in this paper were chosen for their relevance to important medical applications. For tumor cell receptor imaging, an abundant receptor will be present at 100,000 to 600,000 copies on the cell surface. Assuming a cell volume of 1 pL, and no endocytosis, the maximum concentration of contrast agent achievable is 160 nM to  $1 \mu\text{M}$ . As demonstrated in Fig. 5, the anion exchange beads used in this study can be loaded with ICG equivalence throughout this physiologic range. The beads are also available in volumes ranging from 45 pL to 820 nL, corresponding to roughly 45 to 820,000 cells. Pam78-loaded HA also has significant biologic relevance in light of recent reports that the malignant calcification of breast cancer is composed of HA, and not other calcium salts,<sup>14</sup> and since the ICG equivalence<sub>(725–775 nm, 5 mW/cm<sup>2</sup>, >795 nm, 1 mm)</sub> of Pam78-loaded HA is within the range obtained during *in vivo* imaging.<sup>13,23</sup> When combined with our results from tissue autofluorescence measurements, and published values for tissue optical properties,<sup>28</sup> one should be able to use these phantoms to es-

timate, prior to *in vivo* experimentation, the performance of virtually any molecularly targeted NIR fluorophore having similar excitation/emission wavelengths as ICG in DMSO, embedded in virtually any simulated tissue of interest.

We previously described a simultaneous color video/NIR fluorescence reflectance imaging system for intraoperative use and demonstrated its utility in image-guided sentinel lymph node mapping,<sup>29–33</sup> optical angiography,<sup>17,21</sup> and tumor resection (discussed in Ref. 17). Others have described optical tomography systems for detecting embedded NIR fluorescent targets in the human breast (reviewed in Ref. 34). The translation of NIR fluorescence technology to the clinic will require the training of medical technologists (e.g., for tomographic breast imaging) and surgeons (e.g., for intraoperative reflectance imaging systems). Such training should be greatly facilitated by the tissue-like phantoms described in this paper. As optical imaging approaches clinical use, inexpensive training systems that do not require animal or human subjects during the steepest phase of the learning curve will be particularly helpful.

#### Acknowledgments

We thank Barbara L. Clough for editing and Grisel Rivera for administrative assistance. This work was supported by Department of Energy (Office of Biological and Environmental Research) Grant No. DE-FG02-01ER63188, a Clinical Scientist Development Award from the Doris Duke Charitable

Foundation (nonanimal experiments), an Application Development Award from the Center for Integration of Medicine and Innovative Technology (CIMIT) and Grants No. R01-CA-115296 and No. R01-CA-110185 from the National Cancer Institute of the National Institutes of Health to JVF.

## References

1. Y. T. Lim, S. Kim, A. Nakayama, N. E. Stott, M. G. Bawendi, and J. V. Frangioni, "Selection of quantum dot wavelengths for biomedical assays and imaging," *Molecular Imaging* **2**, 50–64 (2003).
2. A. H. Hielscher, A. Y. Bluestone, G. S. Abdoulaev, A. D. Klose, J. Lasker, M. Stewart, U. Netz, and J. Beuthan, "Near-infrared diffuse optical tomography," *Dis. Markers* **18**, 313–337 (2002).
3. E. M. Sevick-Muraca, J. P. Houston, and M. Gurfinkel, "Fluorescence-enhanced, near infrared diagnostic imaging with contrast agents," *Curr. Opin. Chem. Biol.* **6**, 642–650 (2002).
4. V. Ntziachristos, C. Bremer, and R. Weissleder, "Fluorescence imaging with near-infrared light: new technological advances that enable *in vivo* molecular imaging," *Eur. Radiol.* **13**, 195–208 (2003).
5. J. V. Frangioni, "In vivo near-infrared fluorescence imaging," *Curr. Opin. Chem. Biol.* **7**, 626–634 (2003).
6. R. Cubeddu, A. Pifferi, P. Taroni, A. Torricelli, and G. Valentini, "A solid tissue phantom for photon migration studies," *Phys. Med. Biol.* **42**, 1971–1979 (1997).
7. G. Wagnieres, S. Cheng, M. Zellweger, N. Utke, D. Braichotte, J. P. Ballini, and H. van den Bergh, "An optical phantom with tissue-like properties in the visible for use in PDT and fluorescence spectroscopy," *Phys. Med. Biol.* **42**, 1415–1426 (1997).
8. K. M. Quan, G. B. Christison, H. A. MacKenzie, and P. Hodgson, "Glucose determination by a pulsed photoacoustic technique: an experimental study using a gelatin-based tissue phantom," *Phys. Med. Biol.* **38**, 1911–1922 (1993).
9. R. G. Kelly, K. J. Jordan, and J. J. Battista, "Optical CT reconstruction of 3D dose distributions using the ferrous-benzoic-xylene (FBX) gel dosimeter," *Med. Phys.* **25**, 1741–1750 (1998).
10. C. A. Giller, H. Liu, P. Gurnani, S. Victor, U. Yazdani, and D. C. German, "Validation of a near-infrared probe for detection of thin intracranial white matter structures," *J. Neurosurg.* **98**, 1299–1306 (2003).
11. T. Boehm, A. Hochmuth, A. Malich, J. R. Reichenbach, M. Fleck, and W. A. Kaiser, "Contrast-enhanced near-infrared laser mammography with a prototype breast scanner: feasibility study with tissue phantoms and preliminary results of imaging experimental tumors," *Invest. Radiol.* **36**, 573–581 (2001).
12. S. Jiang, B. W. Pogue, T. O. McBride, and K. D. Paulsen, "Quantitative analysis of near-infrared tomography: sensitivity to the tissue-simulating precalibration phantom," *J. Biomed. Opt.* **8**, 308–315 (2003).
13. A. Zaheer, R. E. Lenkinski, A. Mahmood, A. G. Jones, L. C. Cantley, and J. V. Frangioni, "In vivo near-infrared fluorescence imaging of osteoblastic activity," *Nat. Biotechnol.* **19**, 1148–1154 (2001).
14. A. S. Haka, K. E. Shafer-Peltier, M. Fitzmaurice, J. Crowe, R. R. Dasari, and M. S. Feld, "Identifying microcalcifications in benign and malignant breast lesions by probing differences in their chemical composition using Raman spectroscopy," *Cancer Res.* **62**, 5375–5380 (2002).
15. S. A. Prahl, M. J. C. van Gemert, and A. J. Welch, "Determining the optical properties of turbid media by using the adding-doubling method," *Appl. Opt.* **32**, 559–568 (1993).
16. X. Ma, J. Q. Lu, R. S. Brockv, K. M. Jacobs, P. Yang, and X. H. Hu, "Determination of complex refractive index of polystyrene microspheres from 370 to 1610 nm," *Phys. Med. Biol.* **48**, 4165–4172 (2003).
17. A. M. De Grand and J. V. Frangioni, "An operational near-infrared fluorescence imaging system prototype for large animal surgery," *Technol. Cancer Res. Treat.* **2**, 553–562 (2003).
18. S. Ohnishi, S. J. Lomnes, R. G. Laurence, A. Gogbashian, G. Mariani, and J. V. Frangioni, "Organic alternatives to quantum dots for intraoperative near-infrared fluorescent sentinel lymph node mapping," *Molecular Imaging* **4**(3), 172–181 (2005).
19. R. Rajagopalan, P. Uetrecht, J. E. Bugaj, S. A. Achilefu, and R. B. Dorshow, "Stabilization of the optical tracer agent indocyanine green using noncovalent interactions," *Photochem. Photobiol.* **71**, 347–350 (2000).
20. C. Benson and H. A. Kues, "Absorption and fluorescence properties of cyanine dyes," *J. Chem. Eng. Data* **22**, 379–383 (1977).
21. A. Nakayama, F. del Monte, R. J. Hajjar, and J. V. Frangioni, "Functional near-infrared fluorescence imaging for cardiac surgery and targeted gene therapy," *Molecular Imaging* **1**, 365–377 (2002).
22. J. R. English, R. Accorsi, J. D. Idoine, J. A. Parker, J. T. Renze, R. C. Lanza, and J. V. Frangioni, "Sub-millimeter technetium-99m calibration sources," *Mol. Imaging Biol.* **4**, 380–384 (2002).
23. R. E. Lenkinski, M. Ahmed, A. Zaheer, J. V. Frangioni, and S. N. Goldberg, "Near-infrared fluorescence imaging of microcalcification in an animal model of breast cancer," *Acad. Radiol.* **10**, 1159–1164 (2003).
24. X. Intes, J. Ripoll, Y. Chen, S. Nioka, A. G. Yodh, and B. Chance, "In vivo continuous-wave optical breast imaging enhanced with indocyanine green," *Med. Phys.* **30**, 1039–1047 (2003).
25. H. Dehghani, B. W. Pogue, S. P. Poplack, and K. D. Paulsen, "Multiwavelength three-dimensional near-infrared tomography of the breast: initial simulation, phantom, and clinical results," *Appl. Opt.* **42**, 135–145 (2003).
26. N. Iftimia, X. Gu, Y. Xu, and H. Jiang, "A compact, parallel-detection diffuse optical mammography system," *Rev. Sci. Instrum.* **74**, 2836–2842 (2003).
27. J. S. Reynolds, T. L. Troy, and E. M. Sevick-Muraca, "Multipixel techniques for frequency-domain photon migration imaging," *Biotechnol. Prog.* **13**, 669–680 (1997).
28. W. F. Cheong, S. A. Prahl, and A. J. Welch, "A review of the optical properties of biological tissues," *IEEE J. Quantum Electron.* **26**, 2166–2195 (1990).
29. S. Kim, Y. T. Lim, E. G. Soltesz, A. M. De Grand, J. Lee, A. Nakayama, J. A. Parker, T. Mihaljevic, R. G. Laurence, D. M. Dor, L. H. Cohn, M. G. Bawendi, and J. V. Frangioni, "Near-infrared fluorescent type II quantum dots for sentinel lymph node mapping," *Nat. Biotechnol.* **22**, 93–97 (2004).
30. C. P. Parungo, S. Ohnishi, A. M. De Grand, R. G. Laurence, E. G. Soltesz, Y. L. Colson, P. M. Kang, T. Mihaljevic, L. H. Cohn, and J. V. Frangioni, "In vivo optical imaging of pleural space drainage to lymph nodes of prognostic significance," *Ann. Surg. Oncol.* **11**, 1085–1092 (2004).
31. C. P. Parungo, Y. L. Colson, S. W. Kim, S. Kim, L. H. Cohn, M. G. Bawendi, and J. V. Frangioni, "Sentinel lymph node mapping of the pleural space," *Chest* **127**, 1799–1804 (2005).
32. C. P. Parungo, S. Ohnishi, S. W. Kim, S. Kim, R. G. Laurence, E. G. Soltesz, F. Y. Chen, Y. L. Colson, L. H. Cohn, M. G. Bawendi, and J. V. Frangioni, "Intraoperative identification of esophageal sentinel lymph nodes with near-infrared fluorescence imaging," *J. Thorac. Cardiovasc. Surg.* **129**, 844–850 (2005).
33. E. G. Soltesz, S. Kim, R. G. Laurence, A. M. DeGrand, C. P. Parungo, D. M. Dor, L. H. Cohn, M. G. Bawendi, J. V. Frangioni, and T. Mihaljevic, "Intraoperative sentinel lymph node mapping of the lung using near-infrared fluorescent quantum dots," *Ann. Thorac. Surg.* **79**, 269–277; discussion-269–277 (2005).
34. V. Ntziachristos and B. Chance, "Probing physiology and molecular function using optical imaging: applications to breast cancer," *Breast Cancer Res.* **3**, 41–46 (2001).